Supporting information

Synthesis and reversible lithium-ion intercalation of a novel chromium-doped iron phosphate with α-$CrPO_4$ structure

Bulat A. Matsaev[1,], Nikita D. Luchinin[1], Ivan A. Trussov[1], Igor A. Presniakov[2,3], Alexey V. Sobolev[2,3], Alexandr A. Golubnichiy[1], Artem M. Abakumov[1], Evgeny V. Antipov[1,2], Stanislav S. Fedotov[1,*].*

[1]Skoltech Center for Energy Science and Technology, Skolkovo Institute of Science and Technology, Moscow 121205, Russian Federation

[2]Department of Chemistry, Lomonosov Moscow State University, Moscow 119991, Russian Federation

[3]MSU-BIT University, Shenzhen, 517182 Guangdong Province, P. R. China

[*]Corresponding authors: bulat.matsaev@skoltech.ru, s.fedotov@skoltech.ru

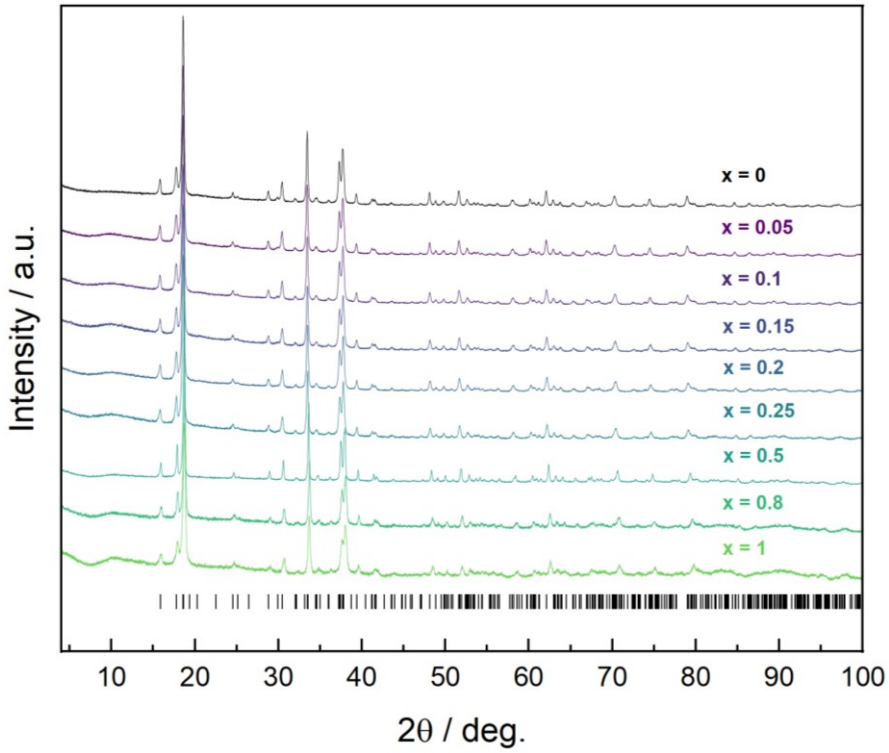

Figure S1. PXRD patterns of $NH_4Fe_{1-x}Cr_xPO_4F$ ($0 \leq x \leq 1$) precursors.

Table S1. Lattice parameters and unit cell volumes of $NH_4Fe_{1-x}Cr_xPO_4F$ ($0 \leq x \leq 1$) solid solutions.

Compounds	*a*, Å	*b*, Å	*c*, Å	*V*, Å^3	GOF	R_{wp}	R_p
NH_4FePO_4F	12.9874(2)	6.4632(1)	10.6334(1)	892.57(2)	1.04	3.54	2.76
$NH_4Fe_{0.95}Cr_{0.05}PO_4F$	12.9834(2)	6.4612(1)	10.6319(1)	891.89(2)	1.05	3.10	2.39
$NH_4Fe_{0.9}Cr_{0.1}PO_4F$	12.9792(3)	6.4587(2)	10.6282(2)	890.94(3)	1.40	3.97	3.12
$NH_4Fe_{0.85}Cr_{0.15}PO_4F$	12.9739(2)	6.4575(1)	10.6244(2)	890.10(3)	1.07	2.69	2.10
$NH_4Fe_{0.8}Cr_{0.2}PO_4F$	12.9702(2)	6.4571(1)	10.6191(2)	889.35(3)	1.02	2.71	2.10
$NH_4Fe_{0.75}Cr_{0.25}PO_4F$	12.9662(3)	6.4552(2)	10.6163(2)	888.59(4)	1.25	3.34	2.63
$NH_4Fe_{0.5}Cr_{0.5}PO_4F$	12.9419(2)	6.4413(1)	10.5897(1)	882.78(2)	1.16	2.64	2.03
$NH_4Fe_{0.2}Cr_{0.8}PO_4F$	12.9119(4)	6.4207(2)	10.5717(3)	876.43(5)	1.00	2.41	1.88
NH_4CrPO_4F	12.8889(6)	6.4067(3)	10.5658(4)	872.48(7)	1.16	2.38	1.86

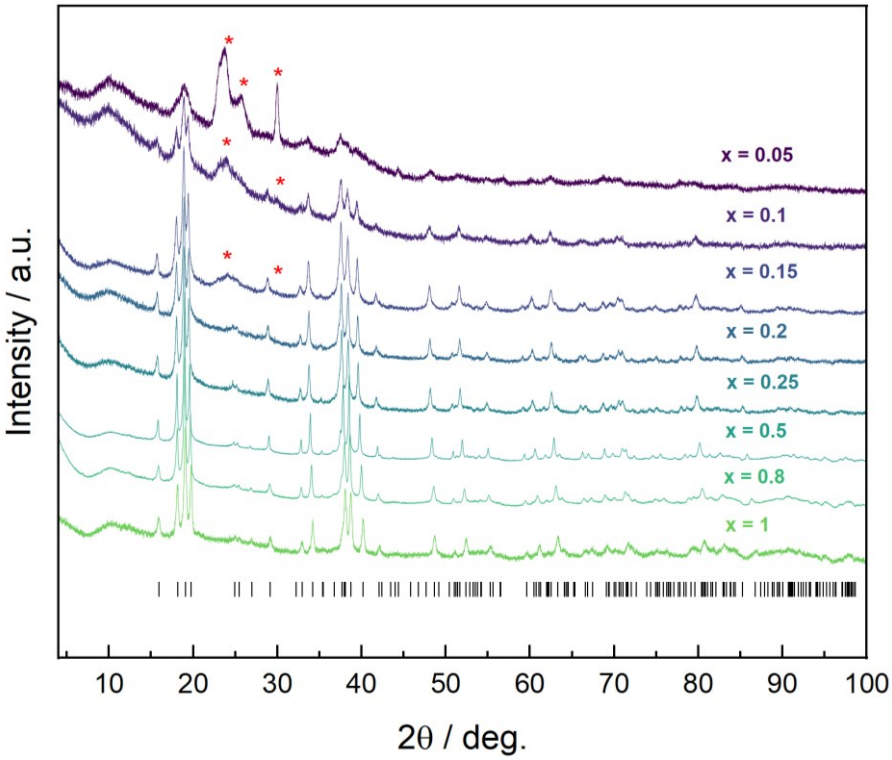

Figure S2. PXRD patterns of $Fe_{1-x}Cr_xPO_4$ ($0.05 \leq x \leq 1$). Red asterisks highlight reflexes of h-$FePO_4$ admixture.

Table S2. Lattice parameters and unit cell volumes of α-$Fe_{1-x}Cr_xPO_4$ ($0.2 \leq x \leq 1$).

Compound	*a*, Å	*b*, Å	*c*, Å	*V*, Å^3	GOF	R_{wp}	R_p
$Fe_{0.8}Cr_{0.2}PO_4$	10.563(2)	13.019(2)	6.3349(9)	871.2(2)	4.02	2.99	2.22
$Fe_{0.75}Cr_{0.25}PO_4$	10.5491(3)	13.0070(4)	6.3361(2)	869.39(6)	2.56	1.25	-
$Fe_{0.5}Cr_{0.5}PO_4$	10.5168(3)	12.9786(4)	6.3311(2)	864.2(1)	1.77	2.00	1.39
$Fe_{0.2}Cr_{0.8}PO_4$	10.4648(3)	12.9230(6)	6.3262(1)	855.5(2)	1.84	2.55	1.85
$CrPO_4$	10.4154(5)	12.8911(6)	6.3090(3)	847.1(1)	1.39	2.91	2.27

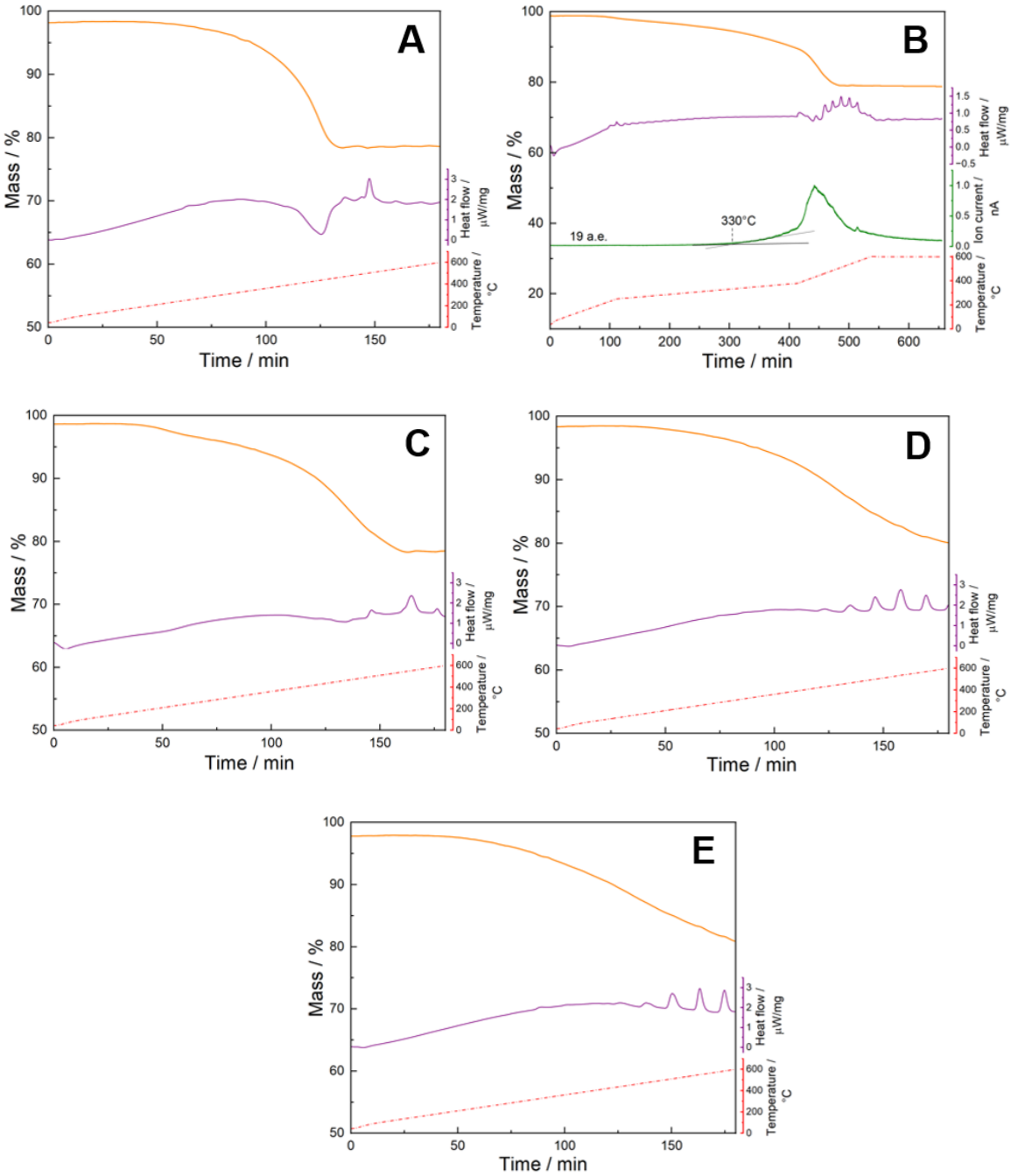

Figure S3. Mass loss (orange), DSC (purple), ion current for 19 a.e. (green) and temperature regime (red) data for (A) NH_4FePO_4F, (B) $NH_4Fe_{0.75}Cr_{0.25}PO_4F$, (C) $NH_4Fe_{0.5}Cr_{0.5}PO_4F$, (D) $NH_4Fe_{0.2}Cr_{0.8}PO_4F$ and (E) NH_4CrPO_4F.

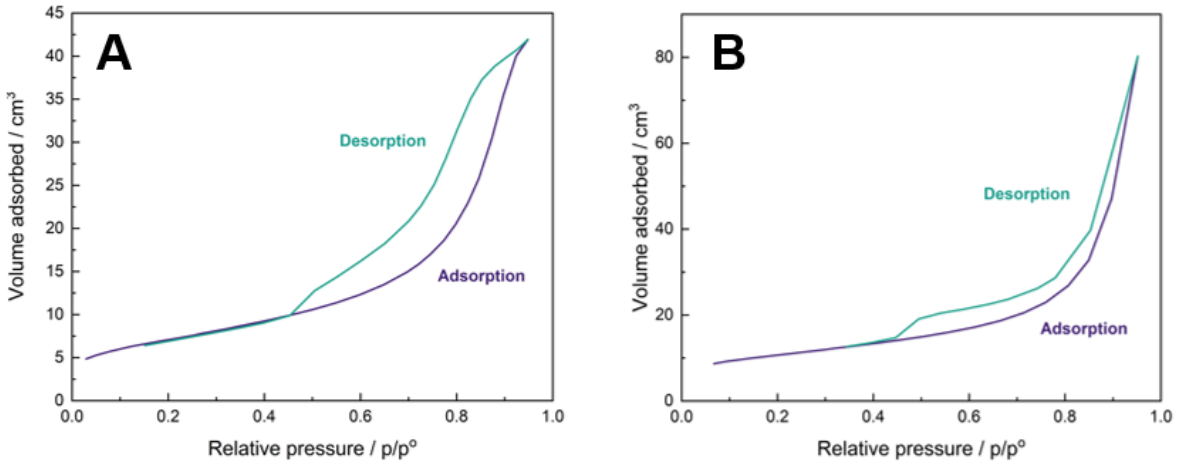

Figure S4. N_2 adsorption and desorption isotherms measured at 77 K for (A) $NH_4Fe_{0.75}Cr_{0.25}PO_4F$ and (B) $Fe_{0.75}Cr_{0.25}PO_4$.

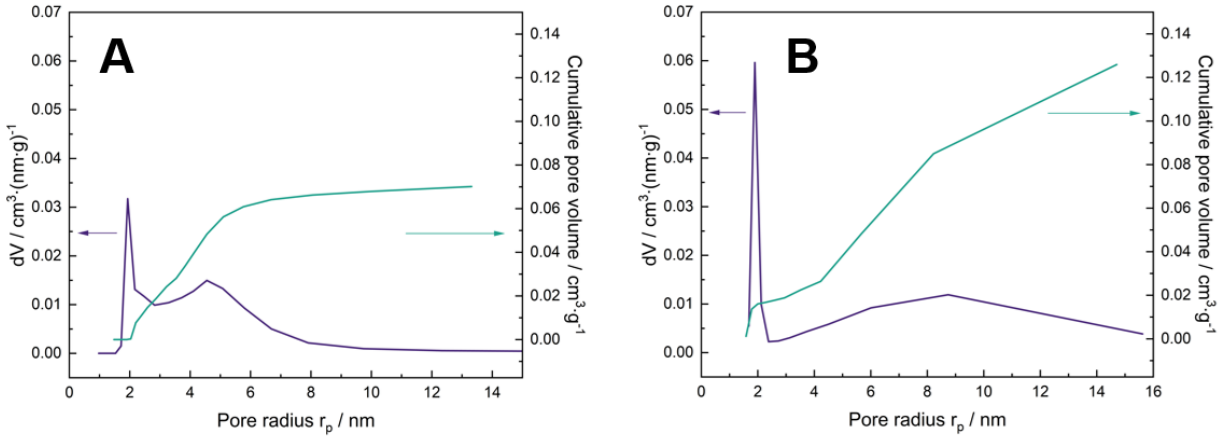

Figure S5. Pore size distribution for (A) $NH_4Fe_{0.75}Cr_{0.25}PO_4F$ and (B) $Fe_{0.75}Cr_{0.25}PO_4$.

Table S3. Chemical composition evaluation based on STEM-EDS data for $Fe_{1-x}Cr_xPO_4$ ($0 \leq x \leq 1$).

Expected chemical formula	Fe : Cr : P : O	Adjusted chemical formula
$FePO_4$	1.00(3) : 0 : 0.97(3) : 3.9(1)	$FePO_4$
$Fe_{0.95}Cr_{0.05}PO_4$	0.96(7) : 0.04(3) : 0.90(4) : 3.8(1)	$Fe_{0.96(7)}Cr_{0.04(3)}PO_4$
$Fe_{0.9}Cr_{0.1}PO_4$	0.91(4) : 0.09(1) : 1.02(3) : 4.0(1)	$Fe_{0.91(4)}Cr_{0.09(1)}PO_4$
$Fe_{0.85}Cr_{0.15}PO_4$	0.87(5) : 0.13(2) : 0.95(3) : 3.9(1)	$Fe_{0.87(5)}Cr_{0.13(2)}PO_4$
$Fe_{0.8}Cr_{0.2}PO_4$	0.82(2) : 0.18(2) : 0.99(1) : 3.9(1)	$Fe_{0.82(2)}Cr_{0.18(2)}PO_4$
$Fe_{0.75}Cr_{0.25}PO_4$	0.76(4) : 0.24(2) : 0.8(1) : 3.5(1)	$Fe_{0.76(4)}Cr_{0.24(2)}PO_4$
$Fe_{0.5}Cr_{0.5}PO_4$	0.52(2) : 0.48(2) : 0.97(2) : 3.9(1)	$Fe_{0.52(2)}Cr_{0.48(2)}PO_4$
$Fe_{0.2}Cr_{0.8}PO_4$	0.22(2) : 0.78(4) : 0.88(5) : 3.8(1)	$Fe_{0.22(2)}Cr_{0.78(4)}PO_4$
$CrPO_4$	0 : 1.00(4) : 0.90(4) : 3.8(1)	$CrPO_4$

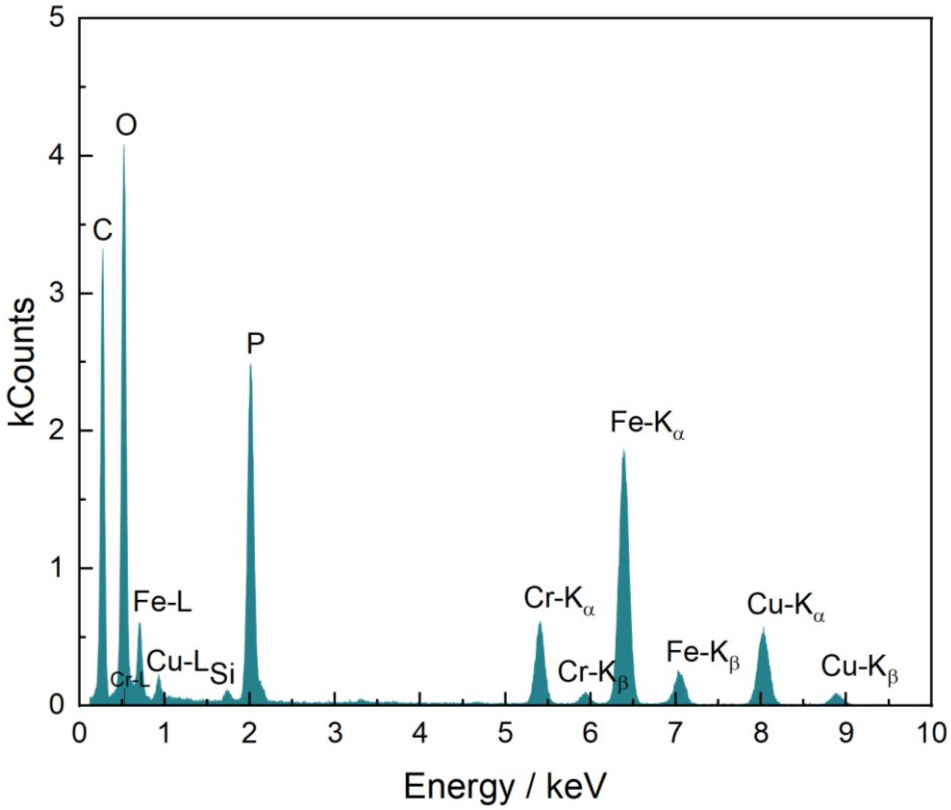

Figure S6. EDS spectrum of α-$Fe_{0.75}Cr_{0.25}PO_4$.

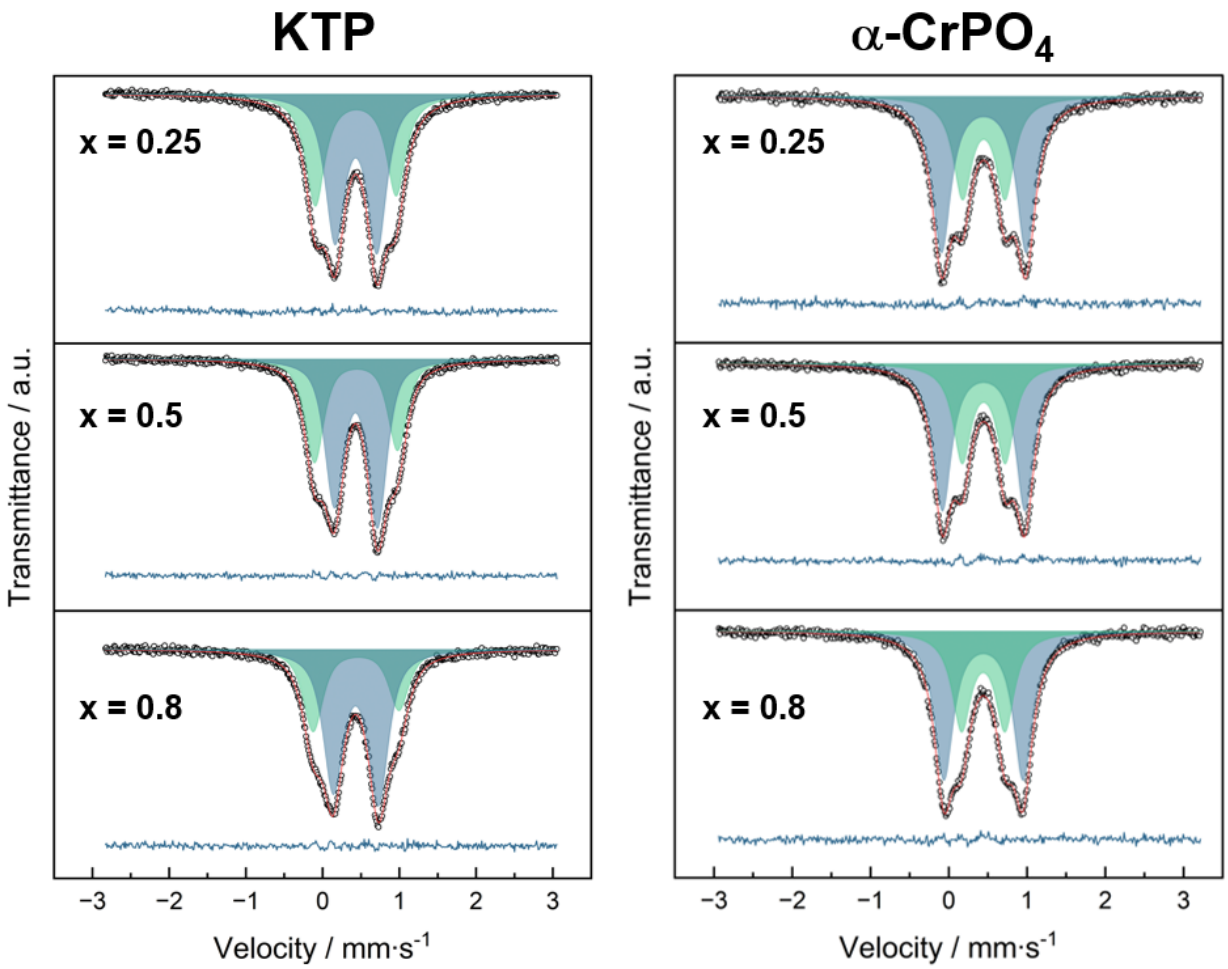

Figure S7. ^{57}Fe Mössbauer spectra (experimental hollow dots) (left) KTP-type $NH_4Fe_{1-x}Cr_xPO_4F$ and (right) α-$CrPO_4$-type α-$Fe_{1-x}Cr_xPO_4$ recorded at room temperature. Solid lines are simulations of the experimental spectra as the superposition of quadrupole doublets Fe1 (green) and Fe2 (blue) corresponding to iron in M1 and M2 positions.

Table S4. Hyperfine parameters of the ^{57}Fe Mössbauer spectra for α-$Fe_{1-x}Cr_iPO_4$ samples at room temperature.

Composition	Site	δ, mm s^{-1}	Δ, mm s^{-1}	Γ, mm s^{-1}	A, %
α-$Fe_{0.75}Cr_{0.25}PO_4$	Fe1 (4b)	0.45(1)	0.54(1)	0.29(1)	38.8(2)
	Fe2 (8g)	0.45(1)	1.086(1)	0.29(1)	61.2(2)
α-$Fe_{0.5}Cr_{0.5}PO_4$	Fe1 (4b)	0.45(1)	0.54(1)	0.28(1)	39.5(3)
	Fe2 (8g)	0.45(1)	1.06(1)	0.28(1)	60.5(3)
α-$Fe_{0.2}Cr_{0.8}PO_4$	Fe1 (4b)	0.44(1)	0.56(1)	0.29(1)	39.3(3)
	Fe2 (8g)	0.44(1)	1.02(1)	0.29(1)	60.7(3)

Calculation of the "lattice" contributions to the EFG

The lattice contribution to the EFG at the Fe^{3+} sites was calculated using a monopole-point model [1]. The monopole contribution (V_{ij}^{mon}) is given by

$$V_{ij}^{\mathrm{mon}} = \sum_k Z_k (3x_{ik}x_{jk} - \delta_{ij} r_k^2)/r_k^5 , \qquad \text{(S1)}$$

where Z_k is the charge and x_{ik} (x_{jk}) are the Cartesian coordinates of the k-th ion with a distance r_k from the origin located at a given site, δ_{ij} is the Kronecher index. The lattice sums were calculated with the spherical boundary method in which the summation is carried out by considering the contributions from all lattice sites inside given radius sphere of 50 Å [1]. The discrepancy between the calculated and observed EFG values is usually attributed to effects of covalency on the EFG at the nucleus [2].

At the final stage, we corrected for shielding effects produced by the own electrons of the iron ions and external charges to obtain the total EFG at the ^{57}Fe nucleus:

$$V_{ii}^{\mathrm{tot}} = (1-\gamma_\infty) V_{ii}^{\mathrm{mon}} , \qquad \text{(S2)}$$

where and γ_∞ = -9.14 is Sternheimer factor [2]. The calculated total contributions to the EFG were diagonalized and the resulting principal values of $\{V_{ii}^{\mathrm{tot}}\}_{i=X,Y,Z}$ were designated according to the usual convention $|V_{ZZ}| \geq |V_{YY}| \geq |V_{XX}|$. The principal components of the EFG tensor were then used to estimate the theoretical quadrupole splitting (Δ^{theor}):

$$\Delta^{\text{theor}} = \frac{eQV_{ZZ}^{\text{tot}}}{2}\sqrt{1+\frac{\eta^2}{3}}\,, \qquad \text{(S3)}$$

where eQ = 0.15 barn [S2] is the ^{57}Fe nucleus quadrupole moment, $\eta = (V_{XX} - V_{YY})/V_{ZZ}$ is the parameter of asymmetry. The calculated values of $\{V_{ii}^{\text{tot}}\}_{i=X,Y,Z}$ and Δ^{theor} for the samples of α-$Fe_{0.76}Cr_{0.24}PO_4$ and NH_4FePO_4F are collected in Tables S5 and S8.

Table S5. Calculated values of the principal components $\{V_{ii}^{\text{lat}}\}_{i=X,Y,Z}$ of the EFG tensor, the asymmetry parameters η^{lat}, and the theoretical quadrupole splittings Δ^{theor} in α-$Fe_{0.75}Cr_{0.25}PO_4$ structure.

Site	$V_{XX}^{\text{lat}}\cdot 10^{21}$ (V/m^2)	$V_{YY}^{\text{lat}}\cdot 10^{21}$ (V/m^2)	$V_{ZZ}^{\text{lat}}\cdot 10^{21}$ (V/m^2)	η^{lat}	Δ^{theor} (mm/s)
Fe1	0.01463	0.31007	-0.32471	0.910	-0.5802
Fe2	0.23094	0.31054	-0.54148	0.147	-0.8596

Table S6. Expanded chemical formula of α-$Fe_{1-x}Cr_xPO_4$ based on the Mössbauer and EDS data.

Composition	Expanded chemical formula
α-$Fe_{0.75}Cr_{0.25}PO_4$	$[Fe1_{0.885}Cr1_{0.115}]_{1/3}[Fe2_{0.698}Cr2_{0.302}]_{2/3}PO_4$
α-$Fe_{0.5}Cr_{0.5}PO_4$	$[Fe1_{0.616}Cr1_{0.384}]_{1/3}[Fe2_{0.472}Cr2_{0.528}]_{2/3}PO_4$
α-$Fe_{0.2}Cr_{0.8}PO_4$	$[Fe1_{0.259}Cr1_{0.741}]_{1/3}[Fe2_{0.200}Cr2_{0.800}]_{2/3}PO_4$

Table S7. Hyperfine parameters of the ^{57}Fe Mössbauer spectra for $NH_4Fe_{1-x}Cr_xPO_4F$ samples at room temperature.

Composition	Site	δ, mm s^{-1}	Δ, mm s^{-1}	Γ, mm s^{-1}	A, %
$NH_4Fe_{0.75}Cr_{0.25}PO_4F$	Fe1 (4*a*)	0.43(1)	1.05(2)	0.30(1)	42.9(6)
	Fe2 (4*a*)	0.43(1)	0.54(1)	0.30(1)	57.1(6)
$NH_4Fe_{0.5}Cr_{0.5}PO_4F$	Fe1 (4*a*)	0.43(1)	1.08(1)	0.30(1)	39.6(5)
	Fe2 (4*a*)	0.43(1)	0.56(1)	0.30(1)	60.4(5)
$NH_4Fe_{0.2}Cr_{0.8}PO_4F$	Fe1 (4*a*)	0.43(1)	1.12(1)	0.31(1)	33.1(1)
	Fe2 (4*a*)	0.43(1)	0.59(1)	0.31(1)	66.9(1)

Table S8. Calculated values of the principal components $\{V_{ii}^{\mathrm{lat}}\}_{i=X,Y,Z}$ of the EFG tensor, the asymmetry parameters η^{lat}, and the theoretical quadrupole splittings Δ^{theor} in NH_4FePO_4F structure.

Site	$V_{XX}^{\mathrm{lat}}\cdot 10^{21}$ (V/m^2)	$V_{YY}^{\mathrm{lat}}\cdot 10^{21}$ (V/m^2)	$V_{ZZ}^{\mathrm{lat}}\cdot 10^{21}$ (V/m^2)	η^{lat}	Δ^{theor} (mm/s)
Fe1	-0.15198	-0.35552	0.50749	0.401	0.8241
Fe2	0.00727	0.21738	-0.22465	0.935	-0.4039

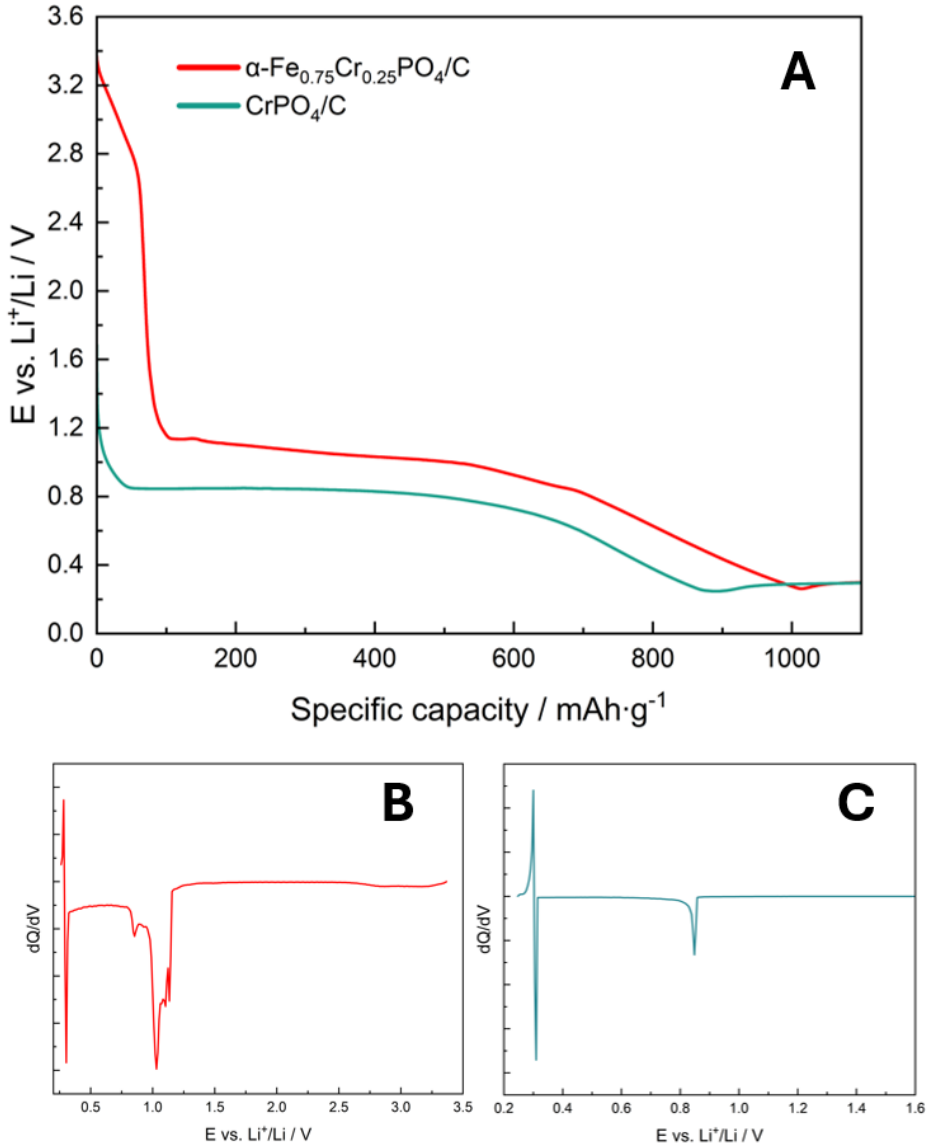

Figure S8. (A) Discharge curves of α-$Fe_{0.75}Cr_{0.25}PO_4$/C and α-$CrPO_4$/C in the low potential region during the first step, and differential curves of (B) α-$Fe_{0.75}Cr_{0.25}PO_4$/C and (C) α-$CrPO_4$/C.

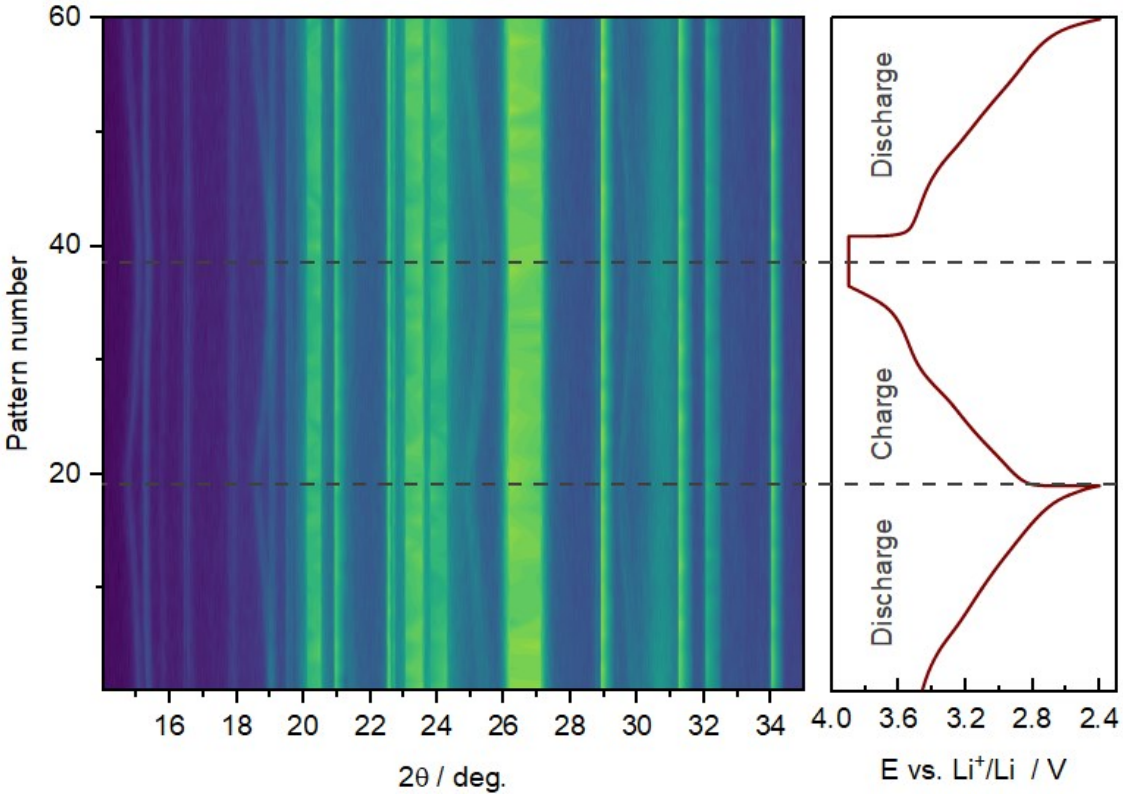

Figure S9. Full *operando* XRD intensity map in the 14.0-35.0 2θ range.

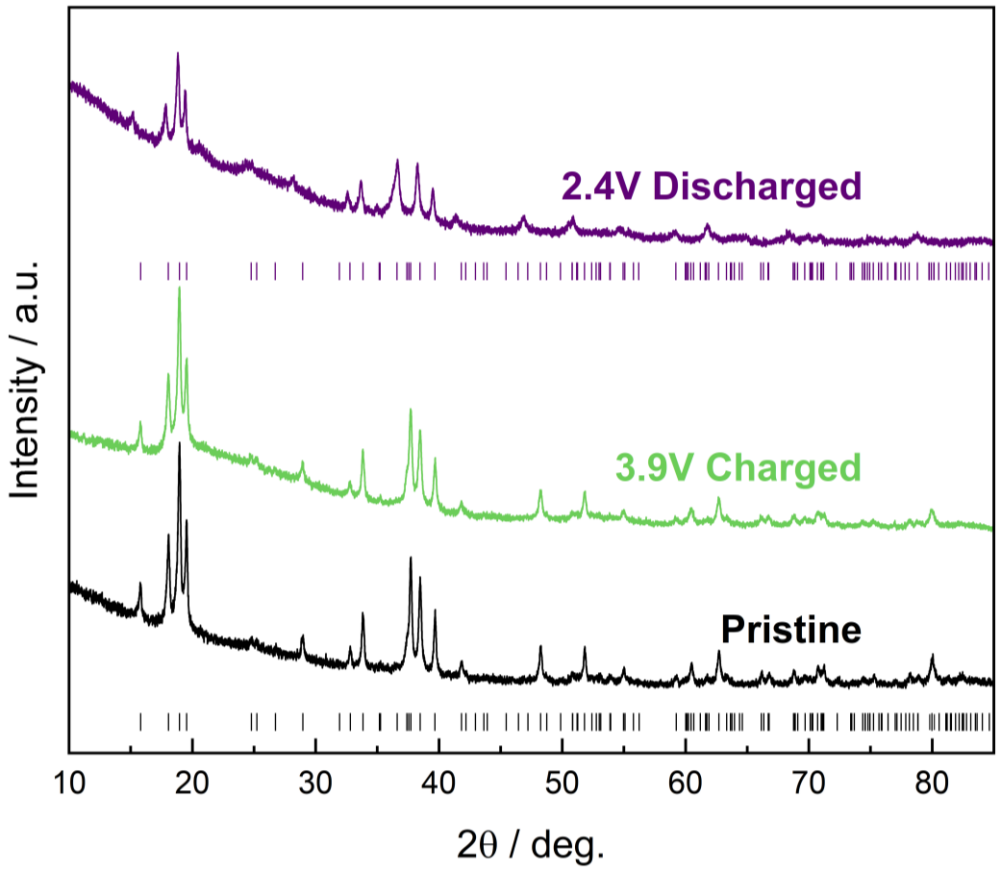

Figure S10. PXRD comparison of *ex situ* charged and discharged samples with the pristine α-$Fe_{0.75}Cr_{0.25}PO_4$/C.

Table S9. Cell parameters of a pristine α-$Fe_{0.75}Cr_{0.25}PO_4$ and charged and discharged electrodes.

	a, Å	*b*, Å	*c*, Å	*V,* Å^3
Pristine	10.5490(3)	13.0073(4)	6.33613(19)	869.41(5)
Ex situ charged at 3.9 V	10.5430(4)	13.0068(5)	6.3372(3)	869.0(1)
Ex situ discharged at 2.4 V	10.5802(7)	13.482(1)	6.3673(5)	908.3(2)

1 Z. M. Stadnik, *J. Phys. Chem. Solids,* 1984, **45**, 311.

2 P. Gütlich, E. Bill and A. X. Trautwein, *Mössbauer spectroscopy and transition metal chemistry: fundamentals and applications*, Springer Science & Business Media, 2010.